Seasonal influence of Indonesian Throughflow in the southwestern Indian Ocean

Lei Zhou and Raghu Murtugudde
Earth System Science Interdisciplinary Center, College Park, Maryland

Markus Jochum
National Center for Atmospheric Research, Boulder, Colorado

Lei Zhou

Address: Computer & Space Sciences Bldg. 2330, University of Maryland, College Park, MD 20742
E-mail: lzhou@atmos.umd.edu
Phone: 301-405-7093

Abstract

The influence of the Indonesian Throughflow (ITF) on the dynamics and the thermodynamics in the southwestern Indian Ocean (SWIO) is studied by analyzing a forced ocean model simulation for the Indo-Pacific region. The warm ITF waters reach the subsurface SWIO from August to early December, with a detectable influence on weakening the vertical stratification and reducing the stability of the water column. As a dynamical consequence, baroclinic instabilities and oceanic intraseasonal variabilities (OISVs) are enhanced. The temporal and spatial scales of the OISVs are determined by the ITF-modified stratification. Thermodynamically, the ITF waters influence the subtle balance between the stratification and mixing in the SWIO. As a result, from October to early December, an unusual warm entrainment occurs and the SSTs warm faster than just net surface heat flux driven warming. In late December and January, signature of the ITF is seen as a relatively slower warming of SSTs. A conceptual model for the processes by which the ITF impacts the SWIO is proposed.

1. Introduction

Sea surface temperature variations in the southern Indian Ocean are generally modest. But they are significantly larger in the southwestern Indian Ocean (SWIO, Annamalai et al. 2003). In an analysis of observational data, Klein et al. (1999) reported that surface heat flux anomalies explain the basin-wide warming over most of the tropical Indian Ocean, the only exception being the SWIO. Masumoto and Meyers (1998) argued that the large SST variations in the SWIO are mainly attributable to the forced Rossby waves propagating from the southeastern Indian Ocean (SEIO). Moreover, due to the Ekman pumping, the SWIO is an upwelling region, where the subsurface thermocline variability also has dramatic influences on the SSTs (Murtugudde and Busalacchi 1999, Schott et al. 2002). Xie et al. (2002) further concluded that much of the SST variability in the SWIO is not due to local winds or surface heat fluxes, but is instead due to oceanic Rossby waves that propagate from the east which affect the temperature of upwelled waters.

The oceanic intraseasonal variabilities (OISVs) have been shown by several recent studies to be important for the heat budget in the oceanic mixed layer, via their impact on horizontal heat transport and related non-linear advective effects (Waliser et al. 2003, 2004; Jochum and Murtugudde 2005). In the southern Indian Ocean, Du et al. (2005) studied the seasonal mixed layer heat budget by analyzing a high-resolution OGCM to argue that the maximum upwelling occurred when the Indonesian Throughflow (ITF) reaches its annual maximum. By comparing the model runs with full-ITF and no-ITF, Hirst and Godfrey (1993) noted that the maximum temperature and salinity perturbations are along the thermocline in the full-ITF run in the region between 28°S and 8°S. In

addition, this region also features strong vertical velocity shears (i.e. the enhanced surface flow/underflow pair). Moreover, the warm advection associated with ITF in their model neutralized the cold upwelling, leading to a slight damping of SST variability off Java and Sumatra (also see Murtugudde et al. 1998). They also found that the residual heat flux in their OGCM was not negligible during boreal winter, which might be attributable to the local intraseasonal variations.

To the best of our knowledge, there have been very few observational and modeling studies of OISVs thus far in the SWIO (e.g., Murtugudde and Busalacchi 1999). We showed in Zhou et al. (2007) that the OISVs are strong from October to January, when they are mainly strengthened by the baroclinic instabilities. Some interesting questions remain unexplored. Since the OISVs in the SWIO are hypothesized to originate from the east (Xie et al. 2002; Zhou et al. 2007), what is the relation between the ITF and the OISVs in SWIO? Do the OISVs in SWIO have a significant impact on local SST variability? In this study, we attempt to address these questions by analyzing an OGCM output along with the World Ocean Atlas data (WOA, Conkright et al. 2002).

In Section 2, the model is described and compared with the satellite SST product (comparisons to altimeter data were presented in Zhou et al. 2007). In Section 3, the westward propagation of the ITF waters and its primary influence in the SWIO is examined. In Section 4, the dynamical influence of ITF in the SWIO is discussed. Section 5 discusses the thermodynamic influence of ITF, focusing on the SST variability and the unusual warm entrainment. A conceptual model for the influence of ITF in SWIO, along with the discussions and conclusions, is presented in Section 6.

2. Model description and comparison

The SWIO has noticeably large OISVs in the southern Indian Ocean (Waliser et al. 2003, Jochum and Murtugudde 2005), which are mainly attributable to the oceanic internal baroclinic instabilities (Feng and Wijffels 2002, Yu and Potemra 2006, Zhou et al. 2007). The wind-forcing used here are weekly mean climatologies which retain very little energy in the intraseasonal band consistent with the hypothesis that the OISVs are generated internally by the ocean. Interannual variability in the atmospheric intraseasonal variabilities (AISVs) may in fact modulate these OISVs especially since the oceanic background state itself varies on interannual time-scales. To simplify the analyses, it is assumed that the interannual variability in the AISV forcing will not affect the basic processes of oceanic internal instabilities and the generation of OISVs. The SST anomalies associated with the OISVs are a significant fraction of the total SST variability in the SWIO which supports our assumption (Jochum and Murtugudde 2005). Therefore, the climatological model outputs are reported in this paper, from which the responses to the intraseasonal atmospheric forcing are largely removed.

The model used is a reduced gravity, sigma-coordinate, primitive equation OGCM, with a horizontal resolution of 1/3º in latitude and 1/2º in longitude over the Indo-Pacific domain covering 32°E-76°W, 30°S-30°N (Murtugudde et al. 1996, 1998). South of 25°S is the sponge layer, where model temperature and salinity are relaxed to WOA (Conkright et al. 2002). There are 15 sigma layers in the vertical below the variable depth mixed layer with a resolution of ~15 m in the thermocline in the SWIO, so that the vertical oscillation in the interior ocean can be adequately resolved. Surface mixed layer is determined by the hybrid mixing scheme of Chen et al. (1994) which explicitly

accounts for the entrainment induced by the surface turbulent kinetic energy, shear-driven dynamic instability mixing, and convective mixing to remove static instabilities. The last sigma-layer thickness is a prognostic variable whereas the other sigma layers are specified constant fractions of the total depth below the mixed layer to the motionless abyssal layer. The model is driven by the climatological weekly NCEP Reanalysis winds as mentioned above (see Murtugudde et al. 2000 for details) with the surface heat fluxes computed by an advective atmospheric mixed layer model which allows SSTs to be directly determined by the variables internally calculated in the model, such as the air temperature and humidity (Seager et al. 1995, Murtugudde et al. 1996). The model outputs for all the analyses presented here are weekly mean fields from the last 20 years of a 270-year simulation.

The OGCM has been reported in many previous applications, demonstrating its ability to simulate the ocean dynamics and thermodynamics reasonably well in the tropical oceans. The mean SSTs (temperatures of the surface mixed layer in the model) and the standard deviations (*STDs*) of the model outputs and the gridded AVHRR data (McClain et al. 1985) are shown in Fig. 1. The model simulations match the satellite observations very well in the tropics, especially the 28°C isotherm in the model, which is the critical threshold for the occurrence of deep convection in the atmosphere, is almost identical to observations. However, there are obvious cold biases. For example, in Bay of Bengal, the simulated SSTs are generally cooler than the observations by ~0.5°C. The maximum cold bias (~1°C) occurs between 10°S and 20°S centered at 15°S, 70°E. The *STDs* of the SSTs are generally small (< 1°C) in the tropical Indian Ocean, where the SSTs are higher than 28°C. In the SWIO, the *STDs* are mostly larger than 1.5°C.

Moreover, the large *STDs* to the northwest of Australia and around the northern tip of Madagascar are also well resolved. These simulated features are consistent with the observations. However, the SST variances are smaller than the observations in the western Arabian Sea and northern Bay of Bengal by ~0.5°C and around 20°S, 80°E by ~1°C. The small SST variances are believed to be mainly attributable to the removal of AISVs from the external wind forcing.

The maximum SST variance around 12°S, which is attributable to the internal variability of the Indian Ocean, has been discussed in Jochum and Murtugudde (2005). In this paper, we focus on the variabilities in the SWIO, which is north to 8°S. Therefore, the cold bias and small SST variance to the south of 10°S do not have significant impact on the following discussions. We can conclude that the model has a good performance for this study on the low latitudes in the Indian Ocean.

3. Westward propagation of the ITF waters

3.1 Indonesian Throughflow in the model

While there is no precise or universally accepted definition of ITF, observational estimates have typically focused on zonal geostrophic transports between Java and Australia in the upper ocean (Meyers 1996). We have used a similar measure to demonstrate the impact of ITF in the Indian Ocean dynamics and thermodynamics (Murtugudde et al. 1996). The zonal transport in the model averaged down to 400 m from 10°S to 15°S along 114°E reaches a maximum of 15 Sv (1 Sv = 10^6 m^3 s^{-1}) in August with an annual mean of about 7 Sv, as in Murtugudde et al. (1998), which is a little smaller than the commonly accepted value of 10 Sv (Gordon 2001) but well within the

uncertainty of the observational and model estimates (Godfrey 1996). The ITF waters at different vertical layers follow different trajectories in the Indian Ocean (Song et al. 2004, Murtugudde et al. 1998). Only the upper layer transports (above ~150 m) are confined between 20°S and 8°N, with further significant influence on the mixed layer in the SWIO, as discussed below. The deep ITF waters, especially below 500 m, mainly flow southward and circulate poleward to 15°S (Song et al. 2004). Therefore, in this study, we only focus on the simulated ITF in the upper 150-meter layer, which is examined more carefully below.

In the upper 150-meter layer, we calculated the potential density, the Ertel potential vorticity (EPV), which is defined as $\frac{(f+\zeta)}{\rho}\frac{\partial\theta}{\partial z}$ where f is the Coriolis parameter, ζ is the relative vorticity, ρ is the density, and θ is the potential temperature; and the zonal temperature advection, $-U\frac{\partial T}{\partial x}$, where U is the zonal velocity and T is the temperature. Associated with the strong westward velocities from July to September (Fig. 2a), the potential density σ_0 is from 22.9 to 23.3 (Fig. 2b), the EPVs are smaller than 2×10^{-3} PVU (1 PVU = 10^{-6} K m^2 kg^{-1} s^{-1}, Fig. 2c), and the warm zonal advection occurs below the surface between 50 m to 100 m (Fig. 2d). The water mass specified by the potential density from 22.9 to 23.3 can be tracked from the SEIO to the SWIO as shown in the *T*-*S* diagram (cross signs in Fig. 3). To the east of 100°E, this water mass is not clearly separable from the ambient water (black and blue circles in Fig. 3), due to a strong mixing in the Indonesian seas (Meyers 1996, Murtugudde et al. 1998). To the west of 100°E, the ITF waters in the upper layer are distinguishable from the ambient Indian Ocean water. The density of the water mass continues to increase during the westward

propagation because of the mixing with the denser ambient Indian Ocean water (Fig. 3). The pathway of the water mass is qualitatively consistent with the Lagrangian trajectory of the upper-layer ITF water shown in Song et al. (2004).

3.2 Westward propagation of the ITF waters

Because the subsurface ITF waters are far from the sea surface and the lateral boundaries, there is no generation or destruction of the potential vorticity after they enter the Indian Ocean. Therefore, projecting the EPV and the horizontal temperature advection onto the $\sigma_0 = 23.3$ surface and following the pathway shown in Fig. 3, one can also track the small EPV ($< 2 \times 10^{-3}$ PVU) and warm advection associated with the ITF from the east to the west across the Indian Ocean basin. Since the ITF water does not propagate strictly westward especially from 80°E to 100°E (Fig. 3), to be more accurate, the horizontal temperature advection, $-U\frac{\partial T}{\partial x} - V\frac{\partial T}{\partial y}$, is shown in Fig. 4(b), although the zonal temperature advection, $-U\frac{\partial T}{\partial x}$, generally dominates. The warm ITF waters are carried westward by the south equatorial currents, as shown with the contours in Fig. 4b. The westward spreading speed of the ITF waters is about 20 cm s^{-1} in the SEIO, but slightly slower in the SWIO (~15 cm s^{-1}). The σ_0 at the sea surface are already larger than 23.3 in the blank regions between 63°E-73°E in Fig. 4, which imply very strong diapycnal mixing blurring the distinction between the ITF water and the ambient denser Indian Ocean water (see Section 4). These regions are also the end of the warm horizontal advection carrying the ITF waters, which imply that the warm subsurface waters are entrained up to the surface (see Section 5.1 for detailed discusses). Since Fig. 4 shows the

westward spreading of the ITF waters in the model explicitly, it will be referred to several times in the following discussions.

3.3 The primary influence of the ITF waters in SWIO

There is a thermocline dome in the SWIO, which is maintained by the Ekman pumping. However, when the ITF waters reach the SWIO, they significantly affect the vertical structure. Because the ITF waters are warmer and more buoyant than the ambient waters, they reduce the vertical stratification as well as the stability in the upper layer from August to December (Fig. 5a). The modification of the vertical structure is mainly attributable to the temperature effect of the ITF waters since the Brunt-Väisälä frequency (N) and the vertical temperature gradients are close to each other (Fig. 5a). Though the ITF waters are also fresher than the ambient waters, the salinity difference is so small that its effect on the vertical stratification is not significant (also see Hirst and Godfrey 1993). The N and the vertical temperature gradients in the upper layer reach their minimum simultaneously in October and early November. Meanwhile, they become larger between the subsurface warm advection and the cold deep ocean waters. This vertical variation of N and the temperature gradients from August to the early December can also be detected in the monthly high-resolution (1/4°) WOA (Conkright et al. 2002; Boyer et al. 2005), which is shown in Fig. 5b. Therefore, the primary influence of the ITF waters on the SWIO is to reduce the vertical stratification leading to significant impacts on the dynamics and thermodynamics in SWIO, which are discussed in the following two sections.

4. Influence of ITF on the dynamics in the SWIO: Scale Selection

In the SWIO, the reduced vertical stratification by the ITF waters is in favor of the baroclinic instability. As a result, the baroclinic energy conversions and the OISVs are enhanced in boreal winter as shown in Zhou et al. (2007). Since the subsurface ITF waters are away from the boundaries, their potential vorticity is conserved during the westward propagation. Following the Eady model described in Vallis (2006, see the Appendix for details), the maximum growth rate of the baroclinically unstable wave is $\sigma_{\max} \approx 0.3U / L_d$, where L_d is the Rossby radius of deformation, the corresponding wavelength of the most unstable wave is $L_{\max} \approx 3.9L_d$. The $L_{\max}$ and $\sigma_{\max}$ are calculated with the model outputs and shown in Fig. 6. In the SWIO, the wavelength of the maximum instability is 500-600 km, which is very close to the wavelength of the OISVs in the SWIO (~650 km, Zhou et al. 2007). The maximum growth rate is mainly between 40-100 days, which is the typical intraseasonal band. Though the theoretical estimations are relatively simple and idealized, they reveal that the dynamical influence of the ITF waters in the SWIO is to reinforce the baroclinic instability and the OISVs via reducing the stratification. Furthermore, the ITF-modified stratification determines the Rossby radius of deformation L_d (the Corriolis parameter and the water depth can be considered as invariable), thereby determine the time-scale and length-scale of the OISVs in the SWIO.

5. Influence of ITF on the SSTs in SWIO

The SST variability in the SWIO is dominated by the net surface heat flux Q_{net}, as shown in Fig. 7. From April to September, the correlation between them is as high as

0.97. However, there are also obvious seasonally-dependent discrepancies between Q_{net} and the SST variability. From October to early December, the SSTs warm faster while in late December and January, they warm slower than Q_{net}. The former difference can clearly be attributed to zonal advection and entrainment, which are significantly influenced by the ITF as discussed in Section 5.1, while the latter difference is assumed to have indirect relations with the ITF, which is discussed in Section 5.2.

5.1 Fast warming SSTs from October to early December

Hirst and Godfrey (1993, 1994) concluded that only in regions with strong upwelling and convective mixing can SSTs be dramatically affected by subsurface temperature perturbations generated by the ITF. The SWIO is just such a region. Due to Ekman pumping, it is an open-ocean upwelling region which is characterized by a shallow thermocline (Reverdin 1987, Murtugudde and Busalacchi 1999, Schott et al. 2002). Surface turbulent kinetic energy tends to deepen the mixed layer in the meantime, rendering the entrainment term to be a significant component of the mixed layer heat budget. The correlation between entrainment and SST variability is 0.8 (Fig. 7). In October after the warm ITF waters reach the SWIO, the water column from 30 m – 70 m (centered at ~55 m) which is just beneath the mixed layer bottom is significantly warmed (Fig. 8). Thus, rather non-intuitively, entrainment acts to warm the mixed layer rather than cool it (Fig. 7).

The anomalous warm entrainment is usually associated with a barrier layer structure, which is an isothermal layer below the density-stratified surface mixed layer (Lukas and Lindstrom 1991, Sprintall and Tomczak 1992) and serves to decouple the

thermodynamics and the mixed layer dynamics. There are multiple processes responsible for the barrier layer formation. For example, Schiller and Godfrey (2003) found that in the central and eastern tropical Indian Ocean, the barrier layer occurs due to the long-term fresh water gains at the surface. Meanwhile, the penetrative solar radiation heats the water below the shallow mixed layer during the clear and calm phase of an intraseasonal event. As a result, the vertical temperature inversion occurs, leading to the warm entrainment. We calculated the barrier layer according to the definition of Sprintall and Tomczak (1992) with the weekly model outputs. The large penetrative solar heating and the barrier layer formation are captured in the central and eastern tropical Indian Ocean (Fig. 9). However in SWIO, the penetrative heating rates are smaller than 0.1 K $month^{-1}$ in October. The mixed layer is quite deep and there is almost no barrier layer (also see Murtugudde and Busalacchi 1999), because the salinity effects on the stratification are negligible (Hirst and Godfrey 1993). Therefore, the genesis mechanism of the warm entrainment in the SWIO is distinct from what was discussed in Schiller and Godfrey (2003). Rather than being heated by the solar penetration, the waters beneath the mixed layer in the SWIO are warmed by the warm ITF waters originating from the SEIO from October to early December (Fig. 8). Moreover, there are cyclonic eddies in the SWIO (ranging from 70°E to 60°E around 8°S), which lead to increased entrainment and SST disturbance (Fig. 10). Consequently, the subsurface warm waters are entrained into the surface mixed layer, leading to fast warming of SSTs. The subsurface warming and the weakening of the stratification tend to enhance the mixed layer deepening and entrainment. During this process, the strong diapycnal mixing blends the ITF waters and the ambient Indian Ocean waters to the extent that the ITF waters lose their *T-S*

properties (blank regions in Fig. 4). Therefore, the influence of the ITF on the SSTs in the SWIO depends on a subtle balance between the stratification and mixing.

Please note that since the subsurface ITF waters are warmer than the Indian Ocean waters above, the temperature inversions do exist in the model outputs. However, the inversions are too weak to initiate the vertical convection by themselves. Eddy kinetic energy (EKE, provided by the baroclinic instability) is still required to break the isopycnal surface and entrain the ITF waters into the upper mixed layer.

5.2 Slow warming SSTs in late December and January

The fast warming SSTs from October to early December are thus attributable to the westward propagation of the warm ITF waters and the subsequent warm entrainment, as discussed above. The warming of SSTs is however slower than Q_{net} from late December to January as seen in Fig. 7. This difference is attributed to the indirect influence of the injection of ITF waters on local vertical processes.

The ITF waters lose their properties of being warmer and fresher after the strong diapycnal mixing from October to early December. Therefore, from late December into January, the subsurface waters significantly cool and the normal vertical stratification resumes (Fig. 8). However, the OISVs enhanced by the ITF-related baroclinic instability still persist during this time, albeit in their decaying phase (Zhou et al. 2007). Therefore, the remaining OISVs provide sufficient EKE to sustain the cold entrainment, which cools the SSTs, or alternatively, slows the rate of warming. After January, the OISVs dissipate completely and no EKE is available to drive entrainment which results in near-zero entrainment in February and March. Therefore, the slow warming of SSTs in SWIO in

late December and January is attributable to the vertical processes influenced by the intrusion of remote ITF waters into the region.

The pronounced cold entrainment from April to June is likely to be attributable to the local Ekman pumping caused by the pronounced wind stress curl (contours in Fig. 4a). However, its influence on the upper layer heat budget is largely neutralized by the meridional warm temperature advection associated with the southward Ekman transport (note the large westward velocities at this time in Fig. 4b), thereby advection has no significant net impact on the SSTs and the SST variation is mainly controlled by Q_{net} (Fig. 7). The local processes at this time of the year are not directly related to the ITF, so the details of this cold entrainment are not discussed further here.

5.3 Relations between thermodynamics and dynamics in the intraseasonal band

The ITF waters can influence both the dynamics and thermodynamics in the SWIO via modifying the vertical stratification as discussed above. Because the maximum growth rate of the unstable waves is in the intraseasonal band and the entrainment is partly sustained by the EKE generated by the baroclinic instability, the intraseasonal entrainment and the intraseasonal sea surface height anomalies (SSHAs) have high correlations, especially in boreal winter of each year. For examples, at 8°S, 63°E, their correlation is 0.6 (Fig. 11). Actually, the correlation between the two is large both in SWIO and SEIO, where the OISVs and the entrainment are closely related to the ITF (Fig. 12, Du et al. 2005, Yu and Potemra, 2006, Zhou et al. 2007). Therefore, in the SWIO, there is a close relation between the thermodynamics and the dynamics in the intraseasonal bands which is responsible for the relatively persistent Bjerknes feedback in

this region (Annamalai et al. 2003, 2005). It should be possible to estimate the intraseasonal heat fluxes associated with these processes, which are not easily observed. But observed quantities such as the intraseasonal SSHAs may provide a useful entry into inverse calculations which is important for understanding the coupled climate interactions in the region which are of significant importance for the rim countries (for e.g., Xie et al. 2002).

6. Conclusions and discussions

When the ITF waters reach the SWIO from August to early December, the primary influence is to reduce the vertical stratification, which is in favor of the baroclinic energy conversions. Consequently, the OISVs are enhanced (Zhou et al. 2007) and their temporal and spatial scales are determined by the ITF-modified stratification. The ITF also has a significant influence on the SSTs in SWIO. From October to early December, the warm ITF waters heat the subsurface waters leading to an unusual warm entrainment which speeds up the SST warming. From late December to January, the warm ITF waters disappear due to the strong diapycnal mixing driven by the baroclinic instability and the subsurface waters become cool. However, the OISV activity still exists supplying the EKE to drive cold entrainment, leading to a relatively slower warming of the SSTs. These processes are attributable to the ITF impact on local processes.

All the influences of the ITF presented in this paper are in fact based on the analyses of a climatological simulation from an OGCM. However, in reality, we believe that the above influence of the ITF waters in SWIO can be even more pronounced if mixing rates are smaller (most models incur excess mixing) and eddies are resolved

explicitly. Gordon et al. (2003) found that during boreal winter, the cold water flows from the Java Sea into the southern Makassar Strait, preventing the warm Pacific water from entering the Indian Ocean and leading to cooler SSTs in the Indian Ocean. Therefore, the warm subsurface waters are more distinguishable against the ambient Indian Ocean water when they reach the SWIO. Moreover, the wind energy is mainly captured by the second baroclinic mode currents in the SEIO (Iskandar et al. 2006), which can supply more energy to the subsurface westward propagation of the ITF waters.

In summary, we propose that in reality, the southern Makassar Strait is like a valve, through which the cold waters from Java Sea flow into the southern Makassar Strait, making the subsurface warm advection of ITF more distinguished compared with the relatively cool SSTs. The winds over the SEIO are like a propeller, which supply energy to the subsurface warm advection in the ocean. The ITF is like a conveyor belt, which carries the variabilities from SEIO to SWIO and the SWIO is like a mixer during boreal winter, where the subsurface water is mixed up into the upper mixed layer and the SSTs are modulated. These processes are sketched in Fig. 13. Of course, these arguments require more tests against observations and model simulations.

As shown in Song and Gordon (2004), the vertical structure of ITF has a significant impact on the stratification and surface heat flux in the Indian Ocean. Potemra et al. (2002) found that the vertical structure of the ITF has large temporal variability. This study argues that the spreading and mixing of the ITF water and its influence on the southern Indian Ocean have a significant seasonal variability. An interesting question still unresolved now is whether the ITF leads to enhanced or diminished ocean heat gain (Song et al. 2004) from the atmosphere. Godfrey (1996) suggested less ocean heat gain

assuming that the temperature of the upwelling water is increased when the ITF is open. While Vranes et al. (2002) suggested increased heat gain arguing that the transport-weighted temperature of the ITF tends to be cooler than the ambient Indian Ocean thermocline water. We do not intend to settle this issue by analyzing the present model output alone. Nonetheless based on the model results, it is very likely that the influence of the ITF on the ocean heat gain depends on the seasonal variability of the subtle balance between the stratification and the mixing. The SSTs warm relatively faster from October to December which should imply a reduced heat gain, while the SST warming is slower in late December into January, which should drive an enhanced heat gain. The role of these processes on the coupled climate variability remains to be explored.

Acknowledgements

This work was supported by NASA Indian Ocean Mesoscale Funding and NOAA Coupled Mesoscale funding. We deeply appreciate the assistance of James Beauchamp and Eric Hackert in the preparation of model outputs. Zhou gratefully acknowledges his NASA Earth System Science Fellowship.

Appendix

Because the subsurface ITF waters are away from the sea surface and the lateral boundaries, their potential vorticity are conversed after they enter the Indian Ocean until they are entrained into the upper mixed layer in the southwestern Indian Ocean (Fig. 4a). Following Vallis (2006), the conservation equation of the potential vorticity is

$$\left(\frac{\partial}{\partial t}+U\frac{\partial}{\partial x}\right)\left(\nabla^2\Psi+\frac{H^2}{L_d^2}\frac{\partial^2\Psi}{\partial z^2}\right)=0,$$

where U is the basic flow, Ψ is the stream function, H is the water depth, $L_d = NH/f$ is the Rossby radius of deformation, N is the Brunt-Väisälä frequency, and f is the Coriolis parameter. The boundary conditions are

$$\left(\frac{\partial U}{\partial z}z-c\right)\frac{\partial\Psi}{\partial z}-\frac{\partial U}{\partial z}\Psi=0,\quad z=0,H,$$

$$\Psi=0,\quad y=0,L.$$

Assuming the wave-like solution in both x- and y- directions

$$\Psi(x,y,z,t)=\psi(z)\sin ly e^{ik(x-ct)},$$

we obtain the dispersion relation of the Eady waves

$$c=\frac{U}{2}\pm\frac{U}{\mu}\left[\left(\coth\frac{\mu}{2}-\frac{\mu}{2}\right)\left(\frac{\mu}{2}-\tanh\frac{\mu}{2}\right)\right]^{1/2},$$

where $\mu = kL_d$. The instability occurs when $\mu > 2.4$. The corresponding growth rate is

$$\sigma=c_i k=\frac{U}{L_d}\left[\left(\coth\frac{\mu}{2}-\frac{\mu}{2}\right)\left(\frac{\mu}{2}-\tanh\frac{\mu}{2}\right)\right]^{1/2},$$

where c_i is the imaginary part of c. The meridional wave number is omitted in the growth rate because it is much smaller than k. The maximum growth rate occurs when

$\mu_{\max} = 1.61$. Accordingly, the wavelength of the maximum instability is $L_{\max} = \frac{2\pi}{k} = \frac{2\pi L_d}{\mu_{\max}} \approx 3.9 L_d$ and the corresponding maximum growth rate is $\sigma_{\max} \approx 0.3U / L_d$.

Reference

Annamalai, H., R. Murtugudde, J. Potemra, S. P. Xie, P. Liu, and B. Wang, 2003: Coupled dynamics over the Indian Ocean: spring initiation of the Zonal Mode. *Deep-sea Res. II*, **50**, 2305-2330.

——, J. Potemra, R. Murtugudde, and J. P. McCreary, 2005: Effect of preconditioning on the extreme climate events in the tropical Indian Ocean. *J. Clim.*, **18**, 3450-3469.

Boyer, T., S. Levitus, H. Garcia, R. A. Locarnini, C. Stephens, and J. Antonov, 2005: Objective analyses of annual, seasonal, and monthly temperature and salinity for the world ocean on a 0.25° grid. Int. *J. Clim.*, **25**, 931-945.

Chen, D., L. M. Rothstein, and A. J. Busalacchi, 1994: A hybrid vertical mixing scheme and its application to tropical ocean models. *J. Phys. Oceanogr.*, **24**, 2156-2179.

Conkright, M. E., J. I. Antonov, O. K. Baranova, T. P. Boyer, H. E. Garcia, R. Gelfeld, D. Johnson, R. A. Locarnini, P. P. Murphy, T. D. O'Brien, I. Smolyar, and C. Stephens, 2002: World Ocean Database 2001 Volume 1: Introduction, U. S. Government Printing Office: Washington, D. C.

Du, Y., T. Qu, G. Meyers, Y. Masumoto, and H. Sasaki, 2005: Seasonal heat budget in the mixed layer of the southeastern tropical Indian Ocean in a high-resolution ocean general circulation model. *J. Geophys. Res.*, **110**, doi:10.1029/2004JC002845.

Feng, M. and S. Wijffels, 2002: Intraseasonal variability in the south equatorial current of the east Indian Ocean. *J. Phys. Oceanogr.*, **32**, 265-277.

Godfrey, J. S., 1996: The effect of the Indonesian Throughflow on ocean circulation and heat exchange with the atmosphere: A review. *J. Geophys. Res.*, **101**, 12217-12238.

Gordon, A. L., 2001: Interocean exchange. Ocean Circulation and Climate, G. Siedler et al., Eds., Academic Press, 303-314.

——, R. D. Susanto, and K. Vranes, 2003: Cool Indonesian throughflow as a consequence of restricted surface layer flow. *Nature*, **425**, 824-828.

Iskandar, I., T. Tozuka, H. Sasaki, Y. Masumoto and T. Yamagata, 2006: Intraseasonal variations of surface and subsurface currents off Java as simulated in a high-resolution ocean general circulation model. *J. Geophys. Res.*, **111**, doi:10.1029/2006JC003486.

Jochum, M. and R. Murtugudde, 2005: Internal variability of Indian Ocean SST. *J. Clim.*, **18**, 3726-3738.

Hirst, A. C. and J. S. Godfrey, 1993: The Role of Indonesian Throughflow in a Global Ocean GCM. *J. Phys. Oceanogr.*, **23**, 1057-1086.

——, 1994: The Response to a Sudden Change in Indonesian Throughflow in a Global Ocean GCM. *J. Phys. Oceanogr.*, **24**, 1895-1910.

Klein, S. A., B. J. Soden, and N.-C. Lau, 1999: Remote sea surface temperature variations during ENSO: Evidence for a tropical atmospheric bridge. *J. Clim.*, **12**, 917-932.

Lukas, R. and E. Lindstrom, 1991: The mixed layer of the western equatorial Pacific Ocean. *J. Geophys. Res.*, **96**, 3343-3357.

Masumoto, Y. and G. Meyers, 1998: Forced Rossby waves in the southern tropical Indian Ocean. *J. Geophys. Res.*, **103**, 27589-27602.

Meyers, G., 1996: Variation of Indonesian Throughflow and the El Niño-Southern Oscillation, *J. Geophys. Res.*, **101**, 12255-12263.

McClain, E. P., W. G. Pichel, and C. C. Walton, 1985: Comparative Performance of AVHRR-Based Multichannel Sea Surface Temperatures, *J. Geophys. Res.*, **90**, 11587-11601.

Murtugudde, R., R. Seager, and A. Busalacchi, 1996: Simulation of tropical oceans with an ocean GCM coupled to an atmospheric mixed layer model. *J. Clim.*, **9**, 1795-1815.

——, A. J. Busalacchi, and J. Beauchamp, 1998: Seasonal-to-interannual effects of the Indonesian throughflow on the tropical Indo-Pacific basin. *J. Geophys. Res.*, **103**, 21425-21441.

——, and ——, 1999: Interannual variability of the dynamics and thermodynamics of the Indian Ocean. *J. Clim.*, **12**, 2300-2326.

——, J. P. McCreary Jr., and A. J. Busalacchi, 2000: Oceanic processes associated with anomalous events in the Indian Ocean with relevance to 1997–1998. *J. Geophys. Res.*, **105**, 3295–3306.

Potemra, J. T., S. L. Hautala, J. Sprintall, W. Pandoe, 2002: Interaction between the Indonesian Seas and the Indian Ocean in Observations and Numerical Models. *J. Phys. Oceanogr.*, **32**, 1838-1854.

Reverdin, G., 1987: The upper equatorial Indian Ocean: The climatological seasonal cycle. *J. Phys. Oceanogr.*, **17**, 903-927.

Schiller, A. and J. S. Godfrey, 2003: Indian Ocean Intraseasonal Variability in an Ocean General Circulation Model. *J. Clim.*, **16**, 21-39.

Schott, F., M. Dengler, and R. Schoenefeldt, 2002: The shallow overturning circulation of the Indian Ocean. *Prog. Oceanogr.*, **53**, 57-103.

Seager, R., M. B. Blumenthal, and Y. Kushnir, 1995: An Advective Atmospheric Mixed-Layer Model for Ocean Modeling Purposes - Global Simulation of Surface Heat Fluxes. *J. Clim.*, **8**, 1951-1964.

Song, Q. and A. Gordon, 2004: Significance of the vertical profile of the Indonesian Throughflow transport to the Indian Ocean. *Geophys. Res. Lett.*, **28**, 1267-1270.

——, ——, and M. Visbeck, 2004: Spreading of the Indonesian Throughflow in the Indian Ocean. *J. Phys. Oceanogr.*, **34**, 772-792.

Sprintall, J. and M. Tomczak, 1992: Evidence of the Barrier Layer in the Surface Layer of the Tropics. *J. Geophys. Res.*, **97**, 7305–7316.

Vallis, G. K., 2006. Atmospheric and Oceanic Fluid Dynamics: Fundamentals and Large-Scale Circulation. Cambridge University Press, 745 pp.

Vranes, K., A. L. Gordon, and A. Ffield, 2002: The heat transport of the Indonesian throughflow and implications for the Indian Ocean heat budget. *Deep-Sea Res.*, **49**, 1391–1410.

Waliser, D. E., R. Murtugudde, and L. Lucas, 2003: Indo-Pacific Ocean Response to Atmospheric Intraseasonal Variability. Part I: Austral Summer and the Madden-Julian Oscillation. *J. Geophys. Res.*, **108**, doi:10.1029/2002JC001620.

——, ——, and ——, 2004: Indo-Pacific Ocean Response to Atmospheric Intraseasonal Variability. Part II: Boreal Summer and the Intraseasonal Oscillation. *J. Geophys. Res.*, **109**, doi:10.1029/2003JC002002.

Xie, S. -P., H. Annamalai, F. A. Schott and J. P. McCreary Jr, 2002: Structure and mechanisms of South Indian Ocean climate variability. *J. Clim.*, **15**, 864-878.

Yu Z., J. Potemra, 2006: Generation mechanism for the intraseasonal variability in the Indo-Australian basin. *J. Geophys. Res.*, **111**, doi:10.1029/2005JC003023.

Zhou, L., R. Murtugudde, and M. Jochum, 2007: Dynamics of the intraseasonal oscillations in the Indian Ocean South Equatorial Current. *J. Phys. Oceanogr.*, in press.

Captions

Figure 1 Mean SSTs of the 20-year model outputs (a) and of AVHRR data averaged from 1992-2005 (b). (c) and (d) are the same as (a) and (b) but for the *STDs*. All fields are °C. The contour interval for the mean SSTs is 1°C, and for the *STDs* is 0.4°C.

Figure 2 Zonal velocity (a), potential density (b), Ertel potential vorticity (c), and zonal temperature advection (d) averaged from 10°S to 15°S along 114°E in three years.

Figure 3 *T*-*S* diagram of the monthly 20-year mean model outputs. The circles represent the *T*-*S* at 20 meters below and above those represented by the crosses in the same color. Each symbol represents *T*-*S* at one specific depth, latitude, and longitude, as shown in the legend. For example, the twelve black crosses represent the *T*-*S* properties at two layers (50 m and 60 m), one longitude point (113°E), and six latitude points (from 12°S to 14°S with a latitudinal resolution of 1/3°).

Figure 4 EPV (a) and horizontal temperature advection (b) projected onto the surface of $\sigma_0 = 23.3$ along 6°S from 63°E-81°E, along 8°S from 81°E-92°E, and along 12°S from 92°E-115°E, which are smoothed with 5° zonal running mean. The latitude shift from 12°S to 6°S follows the spreading of ITF waters shown in Fig. 3. The contours in (a) are the wind stress curl (10^{-6} Pa m^{-1}) and the contours in (b) are the zonal velocities at the surface of $\sigma_0 = 23.3$ in m s^{-1}.

Figure 5 (a) Mean Brunt-Väisälä frequency (shades in 10^{-2} s^{-1}) and the vertical temperature gradient (contours in K m^{-1}) within a rectangular region 6°S-7°S, 63°E-73°E, calculated with the model outputs. (b) The same as (a), but calculated with the monthly high-resolution WOA.

Figure 6 Wavelength of the maximum instability ($L_{max} = 3.9L_d$) in December (a) and the inverse of the corresponding maximum growth rate ($\sigma_{max} = 0.3U/ L_d$) in December (b).

Figure 7 SST variation, net surface heat flux, entrainment, and horizontal temperature advection averaged within a rectangular region 6°S-7°S, 63°E-73°E, which are smoothed with the one-month running mean. Positive values mean that the upper mixed layer gain heat, while negative values mean that the upper mixed layer lose heat.

Figure 8 Temperature variations (color codes) and mixed layer depth (solid line), which are averaged in the region of 6°S-7°S, 63°E-73°E.

Figure 9 Solar radiation penetration heating rate (shades, in the unit of K/month) and the barrier layer depth (contours, in the unit of m) in October.

Figure 10 Weekly mean SSTs (color codes) and the sea surface velocities (vectors) from Nov. 16 to Nov. 21 of Year 7, when the warm entrainment reaches the maximum.

Figure 11 Intraseasonal entrainment and intraseasonal SSHAs at 8°S, 63°E for 18 years.

Figure 12 Correlations between the intraseasonal entrainment and the intraseasonal SSHAs, which are statistically significant at the 95% confidence level.

Figure 13 Sketch of the influence of ITF on the SWIO. See the text for detailed descriptions.

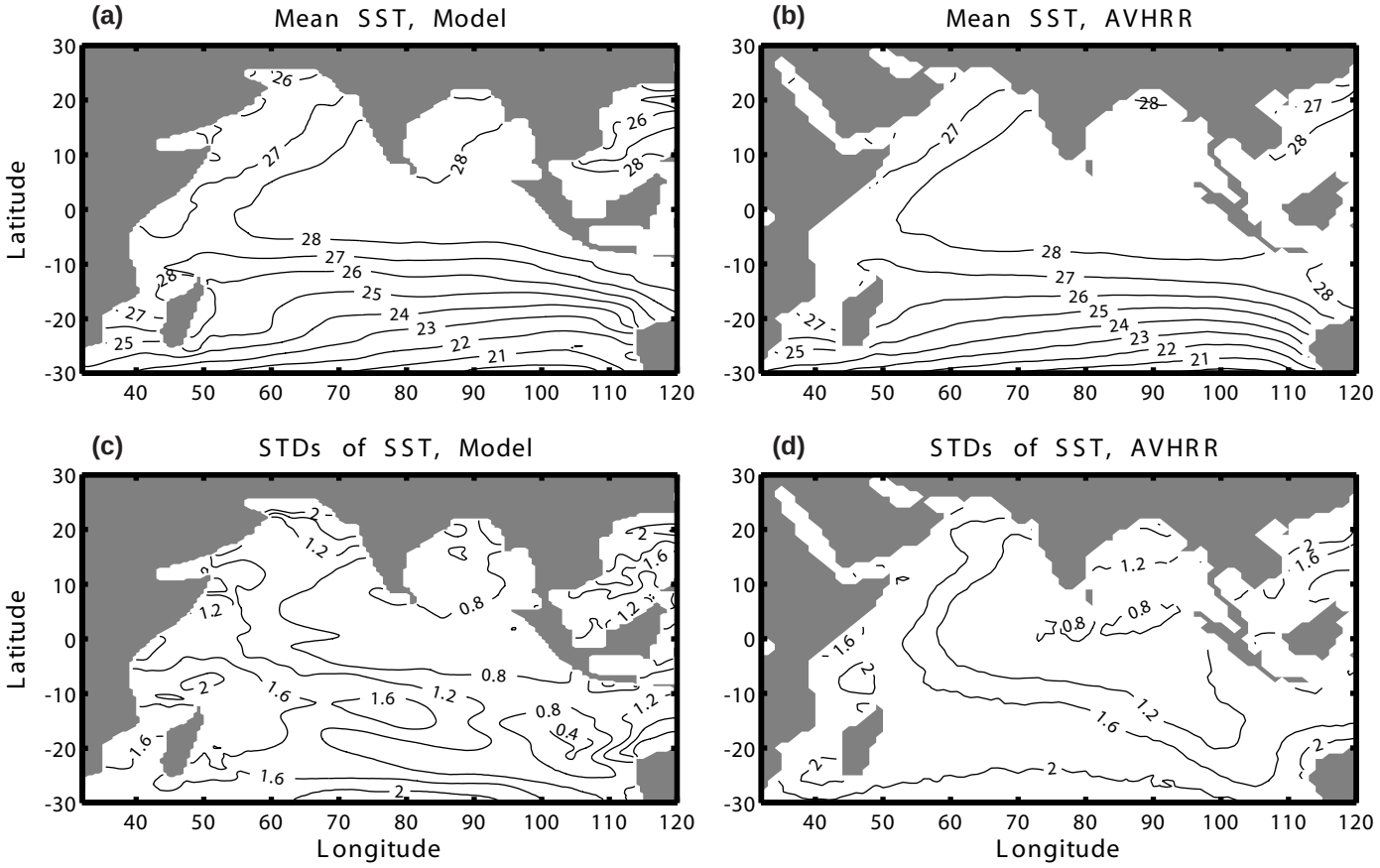

Figure 1 Mean SSTs of the 20-year model outputs (a) and of AVHRR data averaged from 1992-2005 (b). (c) and (d) are the same as (a) and (b) but for the *STDs*. All fields are ℃. The contour interval for the mean SSTs is 1°C, and for the *STDs* is 0.4°C.

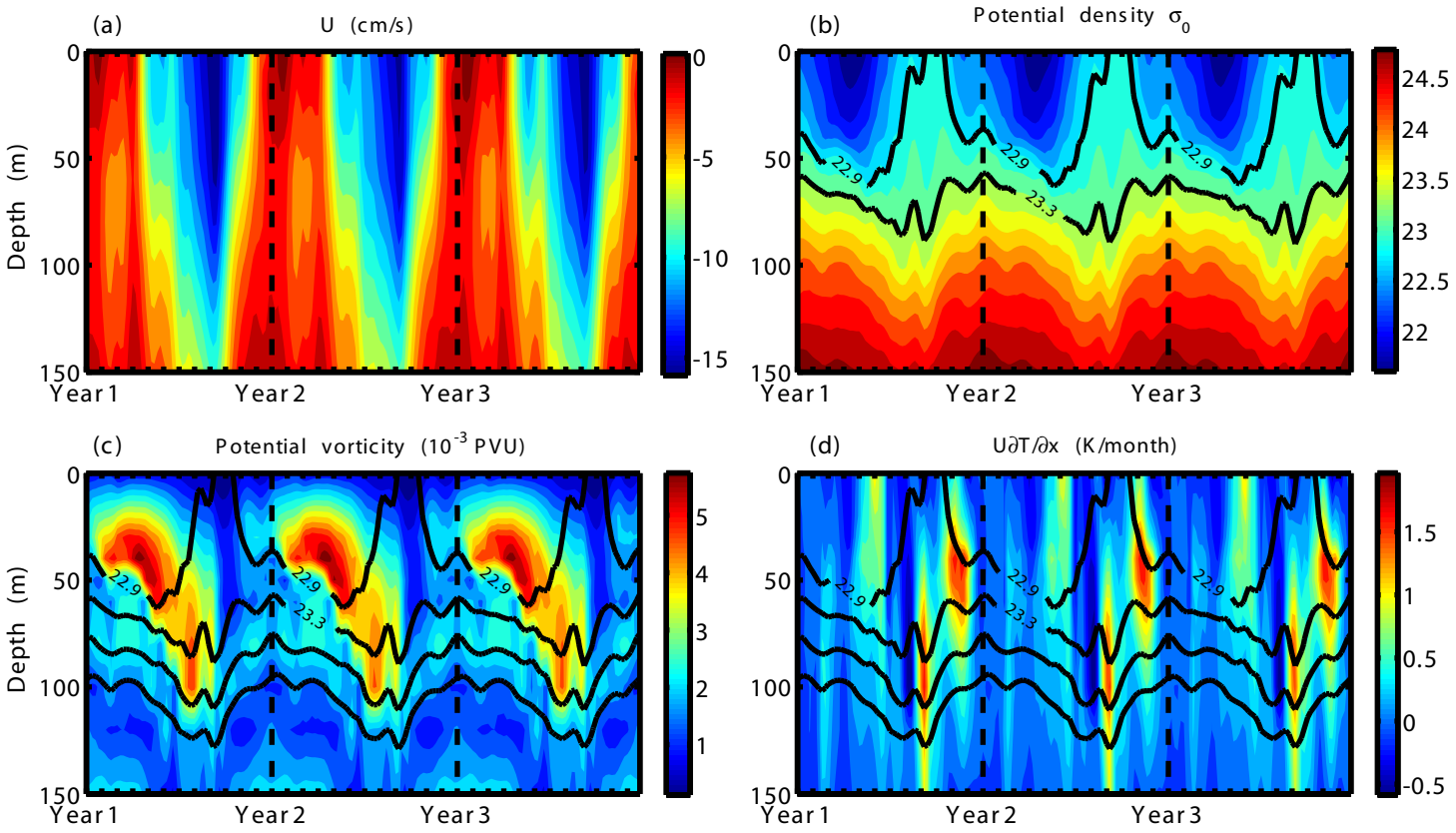

Figure 2 Zonal velocity (a), potential density (b), Ertel potential vorticity (c), and zonal temperature advection (d) averaged from 10°S to 15°S along 114°E in three years.

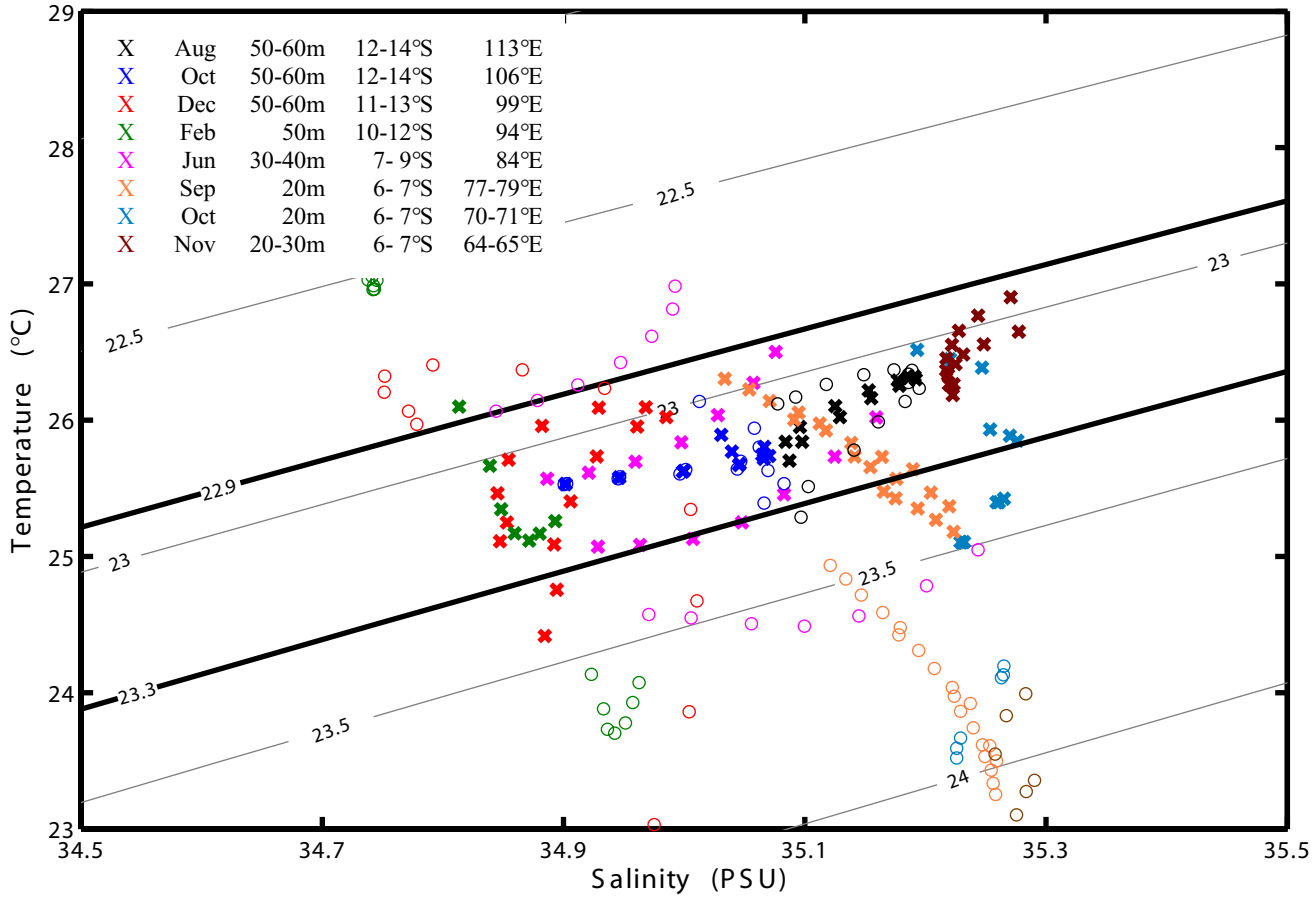

Figure 3 *T-S* diagram of the monthly 20-year mean model outputs. The circles represent the *T-S* at 20 meters below and above those represented by the crosses in the same color. Each symbol represents *T-S* at one specific depth, latitude, and longitude, as shown in the legend. For example, the twelve black crosses represent the *T-S* properties at two layers (50 m and 60 m), one longitude point (113°E), and six latitude points (from 12°S to 14°S with a latitudinal resolution of 1/3°).

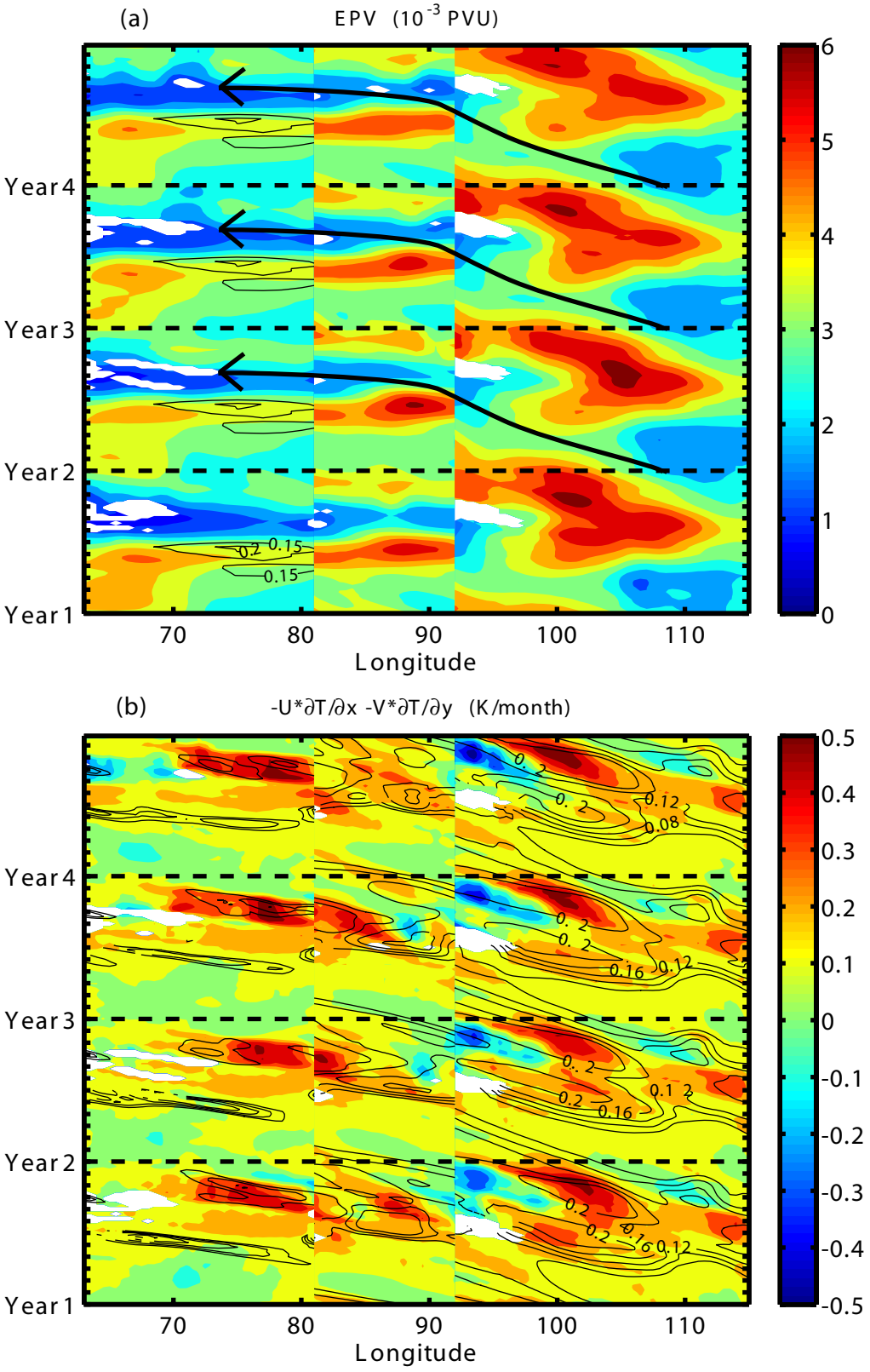

Figure 4 EPV (a) and horizontal temperature advection (b) projected onto the surface of $\sigma_0 = 23.3$ along 6°S from 63°E-81°E, along 8°S from 81°E-92°E, and along 12°S from 92°E-115°E, which are smoothed with 5° zonal running mean. The contours in (a) are the wind stress curl (10^{-6} Pa m^{-1}) and the contours in (b) are the zonal velocities at the surface of $\sigma_0 = 23.3$ in m s^{-1}.

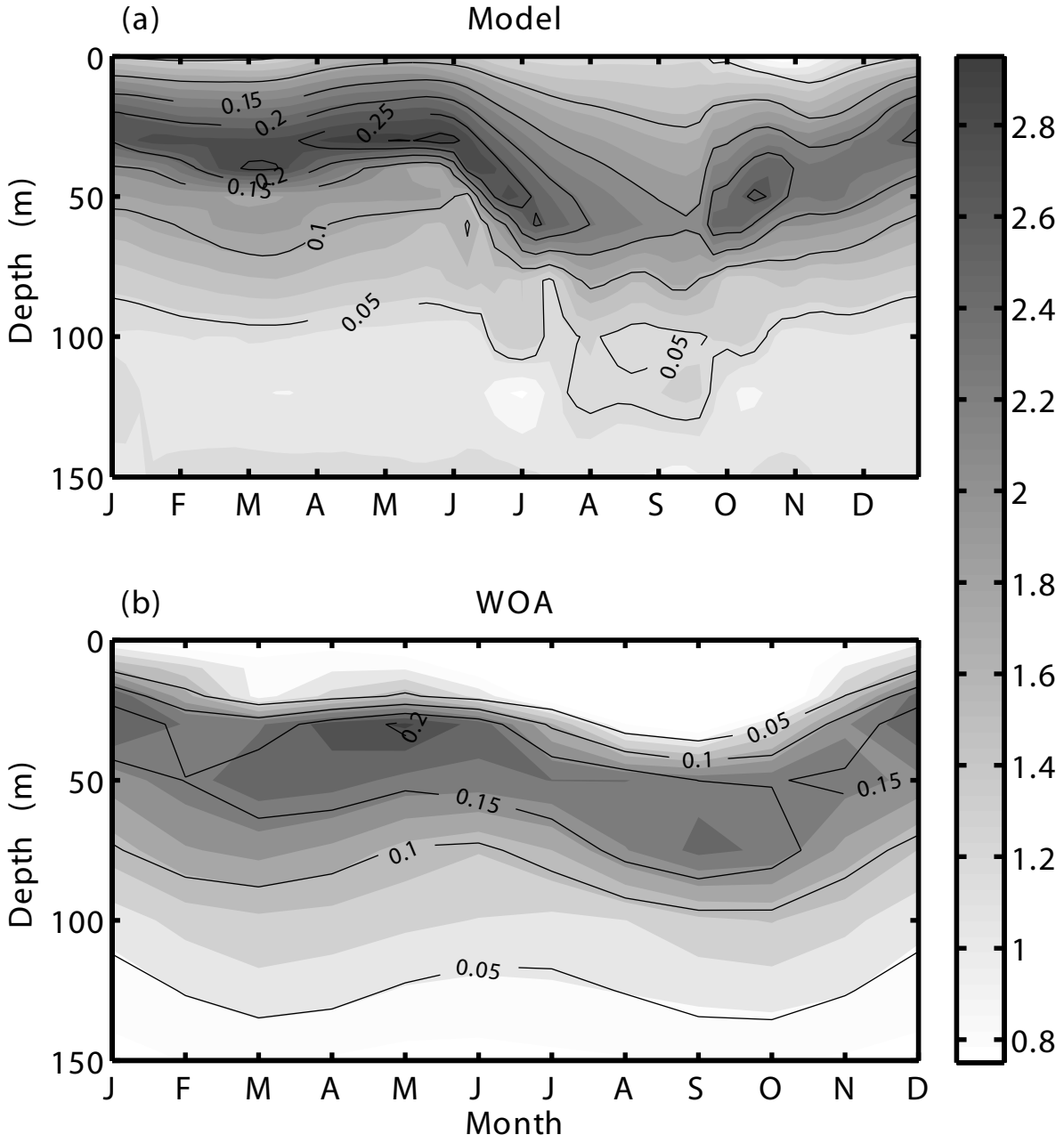

Figure 5 (a) Mean Brunt-Väisälä frequency (shades in 10^{-2} s^{-1}) and the vertical temperature gradient (contours in K m^{-1}) within a rectangular region 6°S-7°S, 63°E-73°E, calculated with the model outputs. (b) The same as (a), but calculated with the monthly high-resolution WOA.

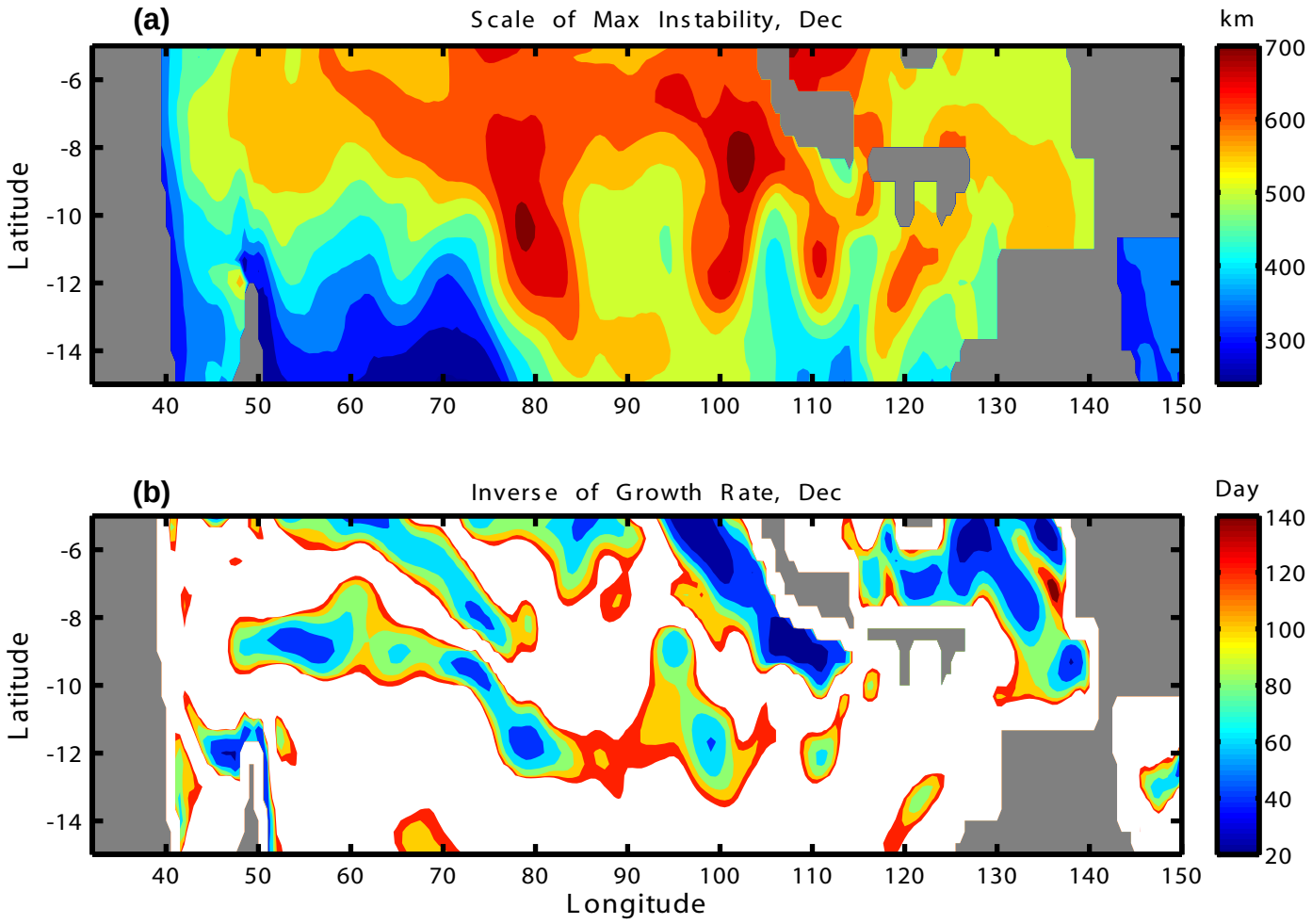

Figure 6 Wavelength of the maximum instability ($L_{max} = 3.9L_d$) in December (a) and the inverse of the corresponding maximum growth rate ($\sigma_{max} = 0.3U/ L_d$) in December (b).

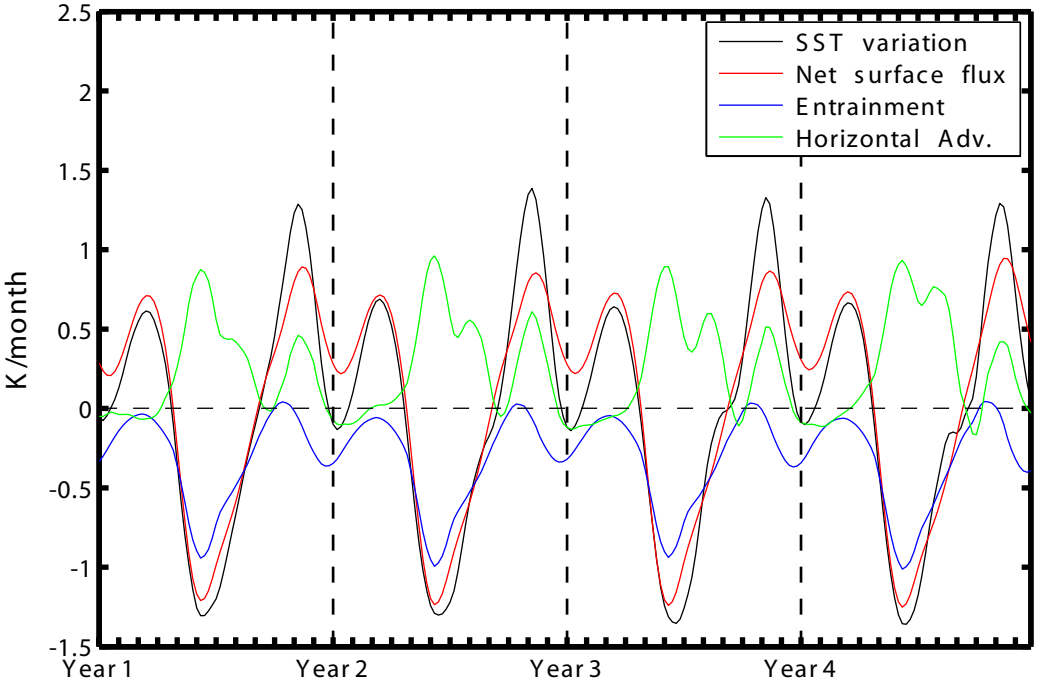

Figure 7 SST variation, net surface heat flux, entrainment, and horizontal temperature advection averaged within a rectangular region 6°S-7°S, 63°E-73°E, which are smoothed with the one-month running mean. Positive values mean that the upper mixed layer gain heat, while negative values mean that the upper mixed layer lose heat.

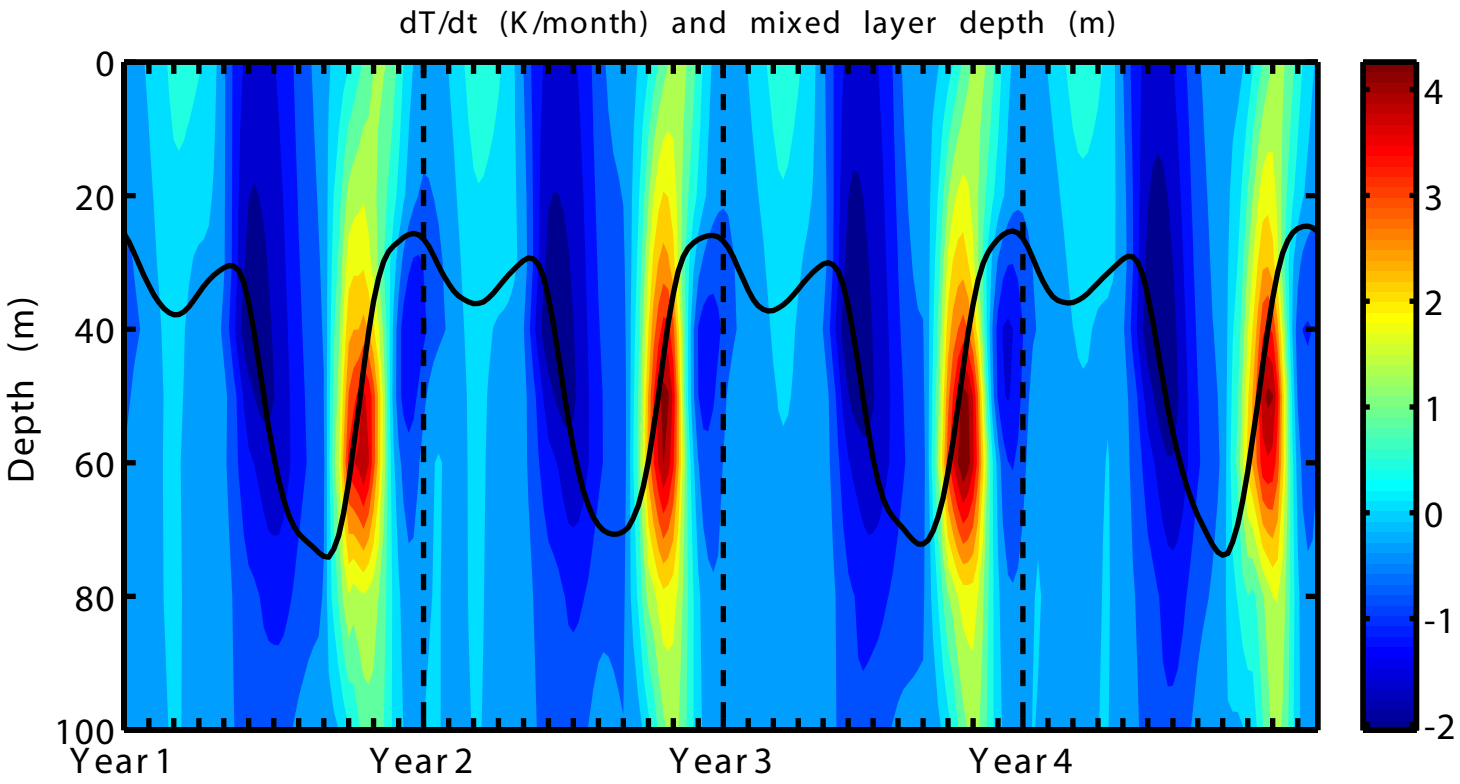

Figure 8 Temperature variations (color codes) and mixed layer depth (solid line), which are averaged in the region of 6°S-7°S, 63°E-73°E.

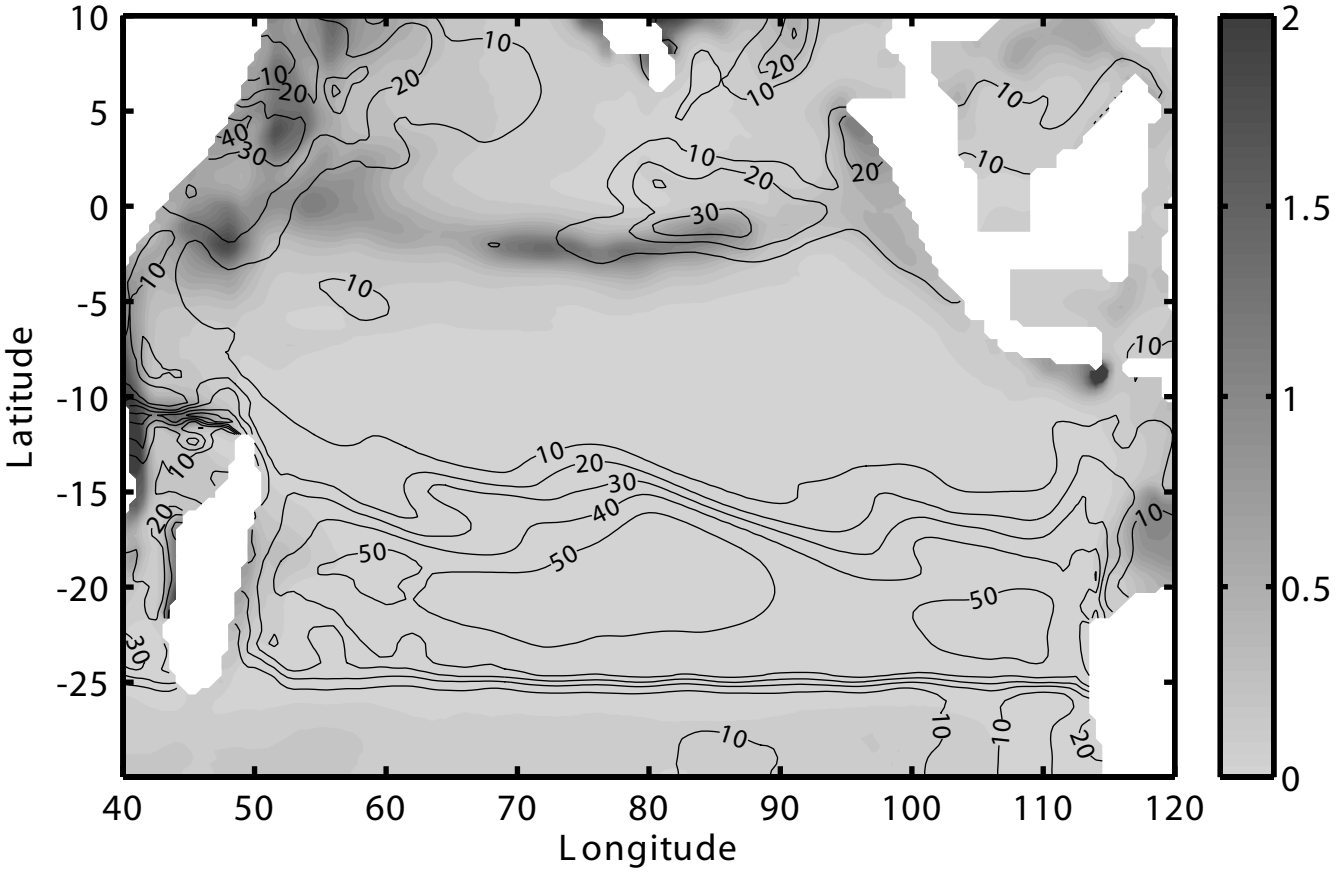

Figure 9 Solar radiation penetration heating rate (shades, in the unit of K/month) and the barrier layer depth (contours, in the unit of m) in October.

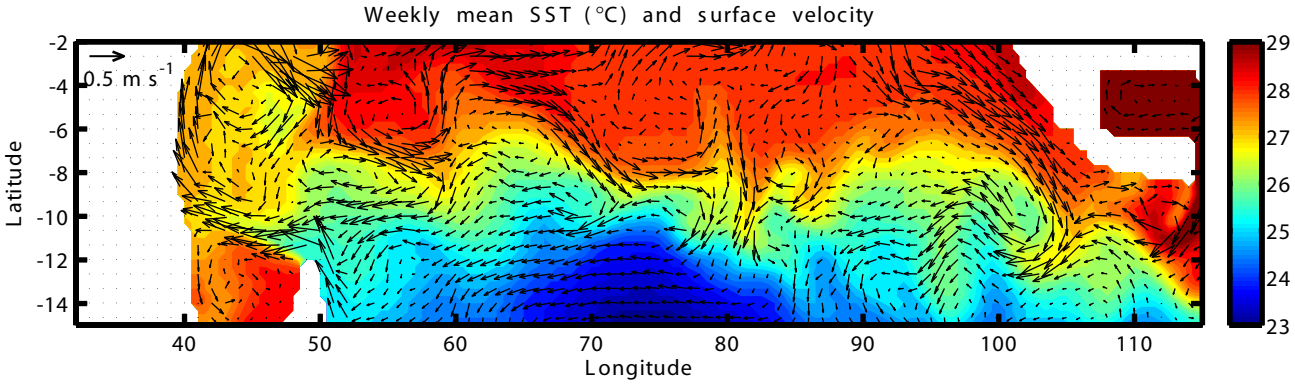

Figure 10 Weekly mean SSTs (color codes) and the sea surface velocities (vectors) from Nov. 16 to Nov. 21 of Year 7, when the warm entrainment reaches the maximum.

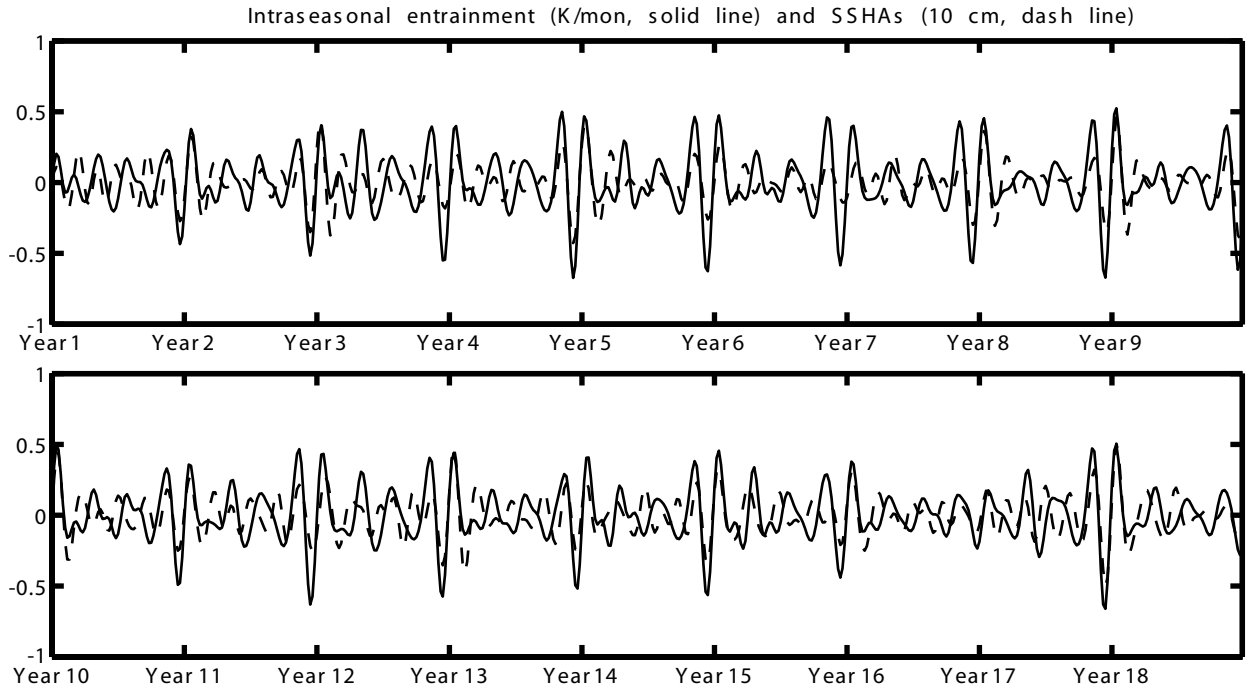

Figure 11 Intraseasonal entrainment and intraseasonal SSHAs at 8°S, 63°E for 18 years.

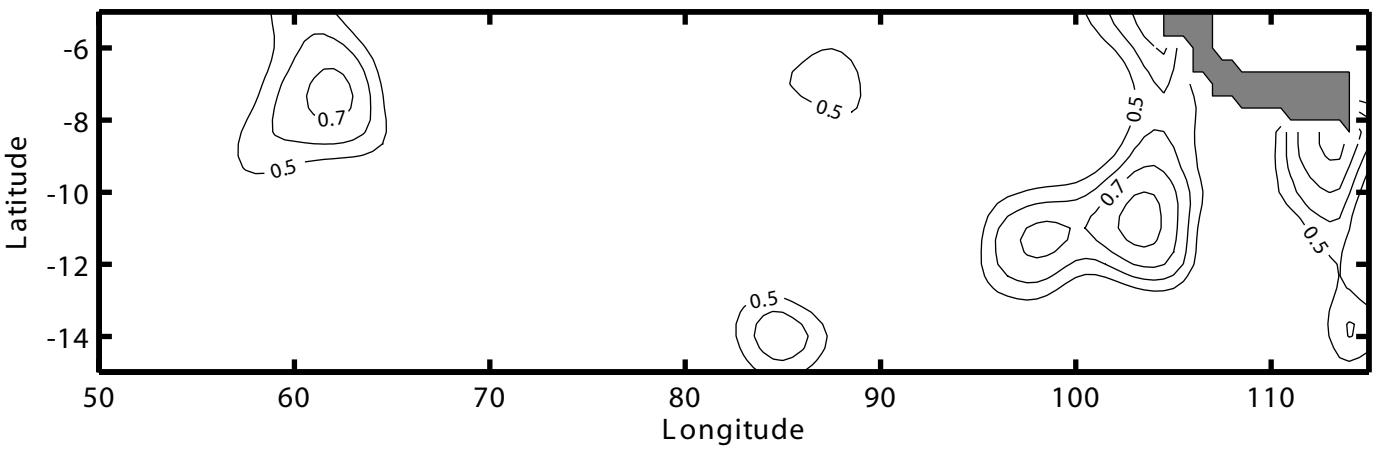

Figure 12 Correlations between the intraseasonal entrainment and the intraseasonal SSHAs, which are statistically significant at the 95% confidence level.

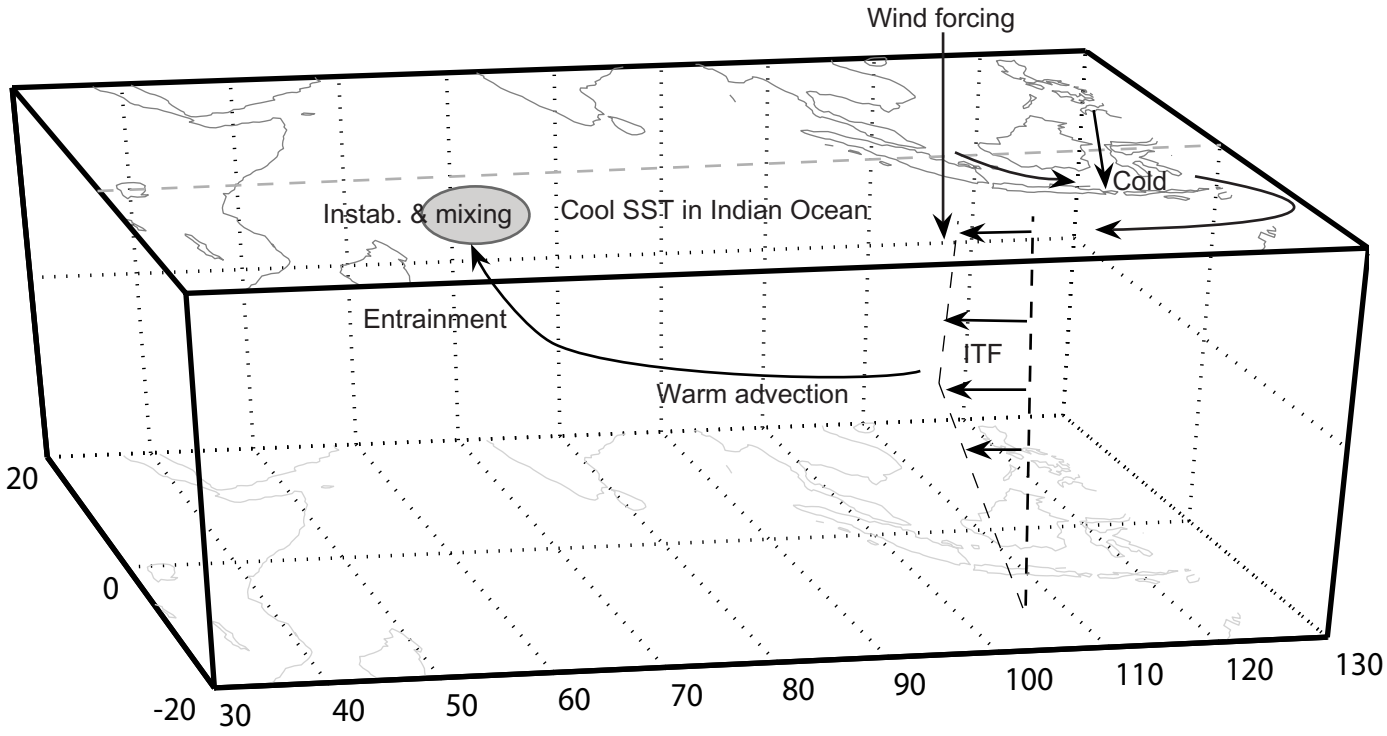

Figure 13 Sketch of the influence of ITF on the SWIO. See the text for detailed descriptions.